

Highly ordered II-VI based organic-inorganic hybrids with over 15-year shelf life

Tang Ye¹, Margaret Kocherga¹, Yi-Yang Sun², Andrei Nesmelov³, Fan Zhang⁴, Xiao-Ying Huang^{5,6}, Jing Li⁵, Damian Beasock¹, Daniel S. Jones³, Thomas A. Schmedake^{1,3}, and Yong Zhang^{1,4*}

¹Nanoscale Science, University of North Carolina at Charlotte, Charlotte, NC 28223, USA.

²State Key Laboratory of High Performance Ceramics and Superfine Microstructure, Shanghai Institute of Ceramics, Chinese Academy of Sciences, Shanghai 201899, China.

³Department of Chemistry, University of North Carolina at Charlotte, Charlotte, NC 28223, USA.

⁴Department of Electrical and Computer Engineering, University of North Carolina at Charlotte, Charlotte, NC 28223, USA.

⁵Department of Chemistry and Chemical Biology, Rutgers University, Piscataway, NJ 08854, USA.

⁶State Key Laboratory of Structural Chemistry, Fujian Institute of Research on the Structure of Matter, Chinese Academy of Sciences, Fuzhou, Fujian 350002, P. R. China.

*Correspondence to: Email: yong.zhang@uncc.edu (Y.Z.)

Organic-inorganic hybrids may offer unique material properties not available from their components. However, they are typically less stable and disordered. Hybrid perovskites are the best examples. Long-term stability study of the hybrid materials, over the anticipated lifespan of a real device, is practically nonexistent. A family of highly ordered II-VI based hybrid semiconductors, first reported around two decades ago, have been shown to possess a number of unusual novel properties and potential applications. Here we show that, using a prototype structure $\text{ZnTe}(\text{en})_{0.5}$, some samples over 15-year old remain as good as freshly made ones in structure and property. This study reveals how the stability of a hybrid material is affected by its intrinsic attribute - formation energy, and extrinsic factors, such as surface and defects.

Organic-inorganic hybrid materials have been explored for a wide range of applications because of their novel and enhanced properties compared to their inorganic counterparts¹⁻⁵. However, they typically exhibit two drawbacks: (1) lower long-term stability than inorganic compounds, which limits the scope of applications; and (2) structural disorder, which affects quantum coherency that is required for various advanced applications, such as quantum computing, as well as very basic material properties, such as electronic conductivity. Hybrid halide perovskites (e.g., MAPbI₃, MA = CH₃NH₃) are perhaps the most extensively and intensively studied hybrid materials. On one hand they have demonstrated extraordinary application potentials in a wide range of applications, in particular photovoltaics (PV) and solid-state lighting (SSL). On the other hand, their long-term stability is known to be relatively poor. By long-term we mean a time scale of one or two decades that is typically expected for (opto-)electronic applications. Despite the major improvement in stability from hours just a few years ago⁶ to currently up to a couple of months⁷⁻⁹, they remain far from adequate for general applications of PV and SSL. One would like to ask: which factors determine the stability of a hybrid material? Systematic long-term stability studies of hybrid materials are understandably rare, since hybrid materials typically do not last long. In general, the stability includes these key aspects: (1) Intrinsic effect, namely the material formation energy calculated as an infinite crystal, which is typically smaller for a hybrid material than its inorganic component. Thus, the consideration lies in whether the binding strength of the hybrid material is adequate for the intended application condition (e.g., operation temperature). (2) The surface or edge effect, which is most relevant to the chemical stability of the material, where degradation can initiate through processes such as oxidation and/or evaporation of the terminating molecules. (3) The structural defects, which tend to provide easier paths for degradation. The improvement in structural and environmental stability for the halide

perovskites benefits from reduction in structural defects and surface passivation⁷⁻⁹. However, the degradation mechanisms are not yet well understood, because of the complexity of these material systems in multiple aspects, such as co-existence of electronic and ionic conductivity, structural disordering, small formation energy or low thermal degradation temperature, but also due to practical limitations of inadequate timespan and control of the degradation processes.

Nevertheless, the low stability of the hybrid perovskites under ambient condition¹⁰ and illumination⁶ is ultimately determined by the intrinsic factor – very low or even negative formation energy^{11,12}.

The II-VI based hybrids were first reported in 2000¹³, including a large number of combinations of II-VI compounds and molecules as well as distinctly different structure types¹⁴. In contrast to most other hybrid materials, such as hybrid perovskites, these II-VI hybrids are highly ordered structures. As a prototype structure, β -ZnTe(en)_{0.5} (en = C₂N₂H₈, ethylenediamine) consists of two-monolayer thick ZnTe (110) slabs interconnected by en molecules forming covalent-like bonding through Zn and N atoms¹³, as shown in Figure 1A. It can be viewed as a hybrid superlattice with the molecule serving as electronic barriers as well as dielectric confinement layers. In contrast to the well-known inorganic semiconductor superlattices (e.g., GaAs/AlAs)¹⁵ where atomic inter-diffusion is practically inevitable within the first few monolayers¹⁶, β -ZnTe(en)_{0.5} has been shown to have crystallinity comparable to most high quality elemental and binary semiconductors, e.g., low temperature Raman linewidth below 1 cm⁻¹^{14,17}. More interestingly, it exhibits various desirable properties, e.g., room temperature excitonic emission due to a large exciton binding energy estimated to be over 200 meV, strongly enhanced optical absorption as high as 10⁶ cm⁻¹¹⁸, broad-range zero-thermal expansion¹⁷, and greatly reduced thermal conductivity¹⁹. These novel properties suggest a number of potential applications,

including room-temperature exciton-polariton condensation, efficient UV emission and detection, and thermoelectrics. Relevant to the growing interest in two-dimensional materials, the inorganic slab is thinner than monolayer transition metal dichalcogenides (TMDs), whereas the organic spacer length or the coupling between the inorganic sheets can be tuned by varying the number of C atoms in $C_nN_2H_{2n+4}$ ($n = 0, 2-4$)²⁰. It is well known that the electronic structure of TMD is extremely sensitive to the layer number for the first few layers²¹, which makes it impractical to stack multiple layers to achieve a “volume” effect when needed (e.g., to enhance optical absorption). The hybrid structures allow stacking desirable number of periods controllably yet with minimal change in electronic structure from that of an individual unit, resembling multiple quantum wells, thus offering an important advantage over the layered inorganic materials. It has recently been demonstrated that one could even exfoliate the thin inorganic slabs individually from these II-VI hybrids²². These unique attributes make β -ZnTe(en)_{0.5} an ideal prototype system for revealing the pertinent mechanisms dictating the long-term stability of the hybrid material and design principles. This work provides a systematic investigation on how the intrinsic and extrinsic mechanisms affect the structural and physical properties of β -ZnTe(en)_{0.5} over one and half decades.

Stability probed by optical spectroscopy

β -ZnTe(en)_{0.5} is an orthorhombic crystal with space group $Pn\bar{m}$, point group D_{2h} , and stacking axis b and in-plane axes a and c , typically found as a thin crystal plate with the b axis aligned with the normal^{13, 18}. Pristine β -ZnTe(en)_{0.5} is a transparent crystal with a bandgap 3.719 eV at 1.5 K¹⁸. It exhibits distinctly different optical properties from those of ZnTe. Fig. 1B - 1D, respectively, compare the spectra of photoluminescence (PL) excited at 325 nm and Raman excited at 532 nm (in small and large frequency regions) of the hybrid samples in pristine and

varying degree of degradation states, with comparison to those of ZnTe. In Fig. 1B, the PL spectrum of a fresh-made sample S19-p (“19” stands for the year of synthesis 2019, “p” for pristine) shows only a single peak (I_{ex}) at 3.569 eV of free exciton emission¹⁸. This hybrid crystal is free of below bandgap defect emission, which is in stark contrast to most high bandgap inorganic semiconductors such as GaN and ZnO where below bandgap defect emission is almost inevitable^{23,24}. In Fig. 1C, the Raman spectrum of S19-p, measured in a backscattering geometry along the b axis and parallel polarization configuration of 45° between a and c axes to reveal a maximum number of Raman modes intrinsic to the hybrid structure, exhibits multiple sharp peaks similar to those reported previously¹⁷ but with two additional lower frequency modes (see Table S1 for Raman mode frequencies and symmetries). The symmetry assignments were obtained by first-principles density-functional theory (DFT) calculations of phonon modes and their Raman tensors. Despite being a much more complex structure (32 atoms/unit cell), the Raman linewidths (measured by full width at half maximum, FWHM) of the hybrid is comparable to that of ZnTe: e.g., 3.2 vs. 3.7 cm^{-1} between the strongest hybrid mode at 133.2 cm^{-1} and ZnTe 1 LO at 205.8 cm^{-1} , indicating a high degree of structural ordering in the hybrid. The Raman spectrum of S19-p in the higher frequency region is shown in Fig. 1D. Because the strong bonding between the ZnTe sheets and en molecules, the ordering also reflects on the en derived Raman modes, where the en modes (see Table S1 for details) are typically shifted in frequency but substantially narrower, compared to those of free-standing en²⁵, for instance, 2869 (FWHM = 5) vs. 2860 (FWHM = 36) cm^{-1} . It is worth noting that β -ZnTe(en)_{0.5} studied here has less Raman modes in the high frequency region than α -ZnS(en)_{0.5} measured previously²⁶, because the α phase has twice as many atoms in the unit cell. Most remarkably, the same intrinsic PL and Raman spectra are observed in samples that are more than a decade old, for example, the PL

spectrum in Fig. 1B, showing even higher intensity, and Raman spectra in Fig. 1C and 1D of sample S07-p that was synthesized in 2007 and had been kept under ambient condition. However, aged samples often exhibited varying degrees of degradation, manifested as changes in both PL and Raman spectrum: the weakening or disappearance of the band edge PL peak and appearance of a broad below bandgap emission band (I_D) in PL, accompanied by the weakening or disappearance of the hybrid Raman modes, and most noticeably the appearance of Raman modes related to metallic Te at ~ 124 and 142 cm^{-1} ²⁷. Representative PL and Raman spectra for a partially degraded sample (S07-pd) and severely degraded sample (S06-d) are shown in Fig. 1B, 1C and 1D, respectively. Such naturally occurring slow degradation can be mimicked by an accelerated process – heating in air, which will be examined later. Degradation is often non-uniform over the surface area of a crystal. For instance, the intrinsic Raman features were observed in some even older samples, such as S03, where adjacent pristine and partially degraded regions co-existed, as shown in Fig. 1E. Although this particular hybrid is not as stable as inorganic semiconductors like Si and GaAs, it is far more stable than most known hybrid materials and it is quite remarkable for some to have a shelf life of over one and half decades! More significantly, these findings indicate that the observed structural degradation of the hybrid may not even be intrinsic in nature rather due to some extrinsic mechanisms, because of the variation in shelf life and the non-uniform degradation.

Crystallinity and stability probed by X-ray diffraction

Judged by the optical signatures, samples like S06-d were severely degraded. However, it was puzzling that these samples still gave rise to the same crystal structure as the pristine sample based on XRD powder diffraction analyses: nearly identical (a , b , c) lattice constants between S19-p and S06-d (see detailed comparisons in Table S2). Figure 2A shows very similar (0n0)

single crystal diffraction peaks between S19-p, S07-p, and S03-d, except for the (020) peak of S03-d being significantly weaker (see Table S3 for tabulated relative intensities with comparison to simulated results). The pristine samples exhibit very high degree of crystallinity, as indicated by the single crystal XRD results of rocking curve or ω scan linewidths (W_{RC}) and ω - 2θ coupled scan linewidths ($W_{2\theta}$). Roughly speaking, W_{RC} measures the lateral uniformity of the crystalline structure, and $W_{2\theta}$ reflects the uniformity of lattice spacing along the stacking direction. For the (020) diffraction, $W_{RC} = 22''$ and $W_{2\theta} = 38''$ for S19-p, as shown in Fig. 2B and 2C, respectively, compared to the results of a high quality ZnTe single crystal with $W_{RC} = 19''$ and $W_{2\theta} = 16.5''$ for the (002) diffraction²⁸. For comparison, the best reported W_{RC} is $35''$ for single crystalline MAPbI₃ and $30''$ for epitaxially grown GaN²⁹. Interestingly, the W_{RC} results of S07-p and S03-d are very similar, $35''$ and $31''$, respectively. These XRD results suggest that despite the signs of degradation in optical spectroscopy, the hybrid samples retained the same crystal structure as a whole. Keep in mind that the mm size x-ray beam not only averaged over the entire sample area (typically a few hundred μm) but also the entire thickness (typically 10-20 μm), whereas the spectroscopy measurements were performed with a confocal optical system that only probed a small volume near the sample surface (on the scale of one μm). Raman depth profiling was conducted for the degraded sample using 532 nm laser that was supposed to be transparent to the pristine material, but the Raman signal decayed quickly into the sample, suggesting the surface region of the degraded sample was highly absorptive. We then cleaved a severely degraded crystal S03-d and performed Raman mapping on the newly exposed edge, shown as an inset in Fig. 2D. It turned out that the body of the about 20 μm thick crystal exhibited the same Raman modes as a pristine sample, and only the regions approximately 2 μm thick from the top and bottom surface were degraded, as shown in Fig. 2D. The results explain the puzzling

“inconsistency” between the optical and XRD results, including the weakened (020) peak of S03-d, corresponding to the largest incidence angle at which more surface region was probed. The observation of the Te modes from the surface region of the “degraded” hybrid is similar to thermally oxidized ZnTe where the top layer consists of amorphous ZnO and nanoscale Te domains³⁰. The observations seem to suggest that the degradation of the hybrid is caused by surface oxidation, as to be confirmed next, that occurs in most non-oxide semiconductors. We may further speculate that a terminating layer of en molecules might prevent the surface from oxidation, a self-passivation effect. However, the oxidation process might initiate at a defective surface or a region with structural defects. This understanding is consistent with the observed variation in shelf life and degradation inhomogeneity. We have also noticed that the edges of a newly synthesized crystal tend to degrade faster than the top surface, because the edges are not terminated by en molecules.

Stability probed by surface analyses

To verify the oxidation process and degradation mechanism, we performed surface analyses using scanning electron microscopy (SEM), energy-dispersive X-ray (EDX) analysis, and X-ray photoelectron spectroscopy (XPS) on different hybrid samples. Figure 3A-3E shows the SEM images obtained for S19-p, S07-p, S03-d, and S19-th (thermally oxidized at 190°C for 20 minutes), and ZnTe, respectively, taken from smooth and clean areas of the samples where optical measurements were conducted. The O:Zn ratio obtained from the EDX analysis is shown with each SEM image. The original EDX spectra are depicted in Figure S2. The comparison reveals a steady increase in oxygen content on the surface with increasing level of degradation, for instance, O:Zn = 0.05 for S19-p and 1.08 for S03-d. These results qualitatively support the proposed degradation mechanism of surface oxidation. XPS data further corroborate these

results. We measured depth-resolved XPS spectra for S19-p, S06-d, and ZnTe by applying in-situ Ar etching, with the results shown, respectively, in Figs. 3F-3H near the energies of two Te 3d transitions. Additional scans of a broader energy range can be found in Figure S3. For S19-p, on the non-etched surface, two peaks were at 576.5 eV ($3d_{5/2}$) and 586.9 eV ($3d_{3/2}$), similar to a naturally oxidized ZnTe in air as reported in the literature³¹; after etching, two new peaks emerged on the lower energy sides respectively at 573.8 eV ($\delta E = - 2.7$ eV) and 584.2 eV ($\delta E = - 2.7$ eV), and after about 15 second etching (or removal of around 150 nm top layer), the high energy peaks disappeared and the new peaks reached saturated intensities. Similar shifts were observed in ZnTe, but the transition energies for pure ZnTe are slightly lower than in the hybrid, by about 0.8 eV. The difference can be understood by the fact that the Te bonding situations are different in the two structures: with each Te bonding to only three Zn in the hybrid and four Zn in ZnTe. For the severely degraded sample, a similar trend was observed, but a much longer etching time (170 s, approximately corresponding to 1.7 μm in depth) was required to reach a steady state, which suggests a thicker oxidized layer on this severely degraded sample and is consistent with the cleaved edge Raman results (Fig. 2D). The remaining weak oxidation peaks after etching indicates that oxidation might have somewhat penetrated into the deeper volume of the crystal. Note that similar to XRD, XPS probes a large area due to its macroscopic beam size, therefore, the results could be affected by the embedded extended defects and surface contamination, whereas micro-Raman and EDX are able to analyze visually perfect regions. We note that even the new sample S19-p had a thin oxide layer, although showing no effect in optical spectroscopy after being kept in air for one year. The existence of the pristine area in S03 seems to suggest that the oxidation process is self-limiting, if no structural defects, as in most non-oxide inorganic semiconductors.

Thermal stability in different environments

Thermal stability is a measure of the bonding strength, and important for device application because of a self-heating effect under the operation condition. Thermal stability study was performed in both air and N₂ protected condition on newly made crystals in two ways: (1) By heating one single piece of the crystal using a heating stage with a small heating chamber from 40 to 500 °C while monitoring with Raman spectroscopy in-situ. (2) By performing thermogravimetric analysis (TGA) to a collection of small crystals. In Raman, significant difference in thermal degradation was observed between heating in air or N₂ until approximately 150 °C. Figure 4A shows the evolution of the Raman spectra while heated in air (spectra at more temperature points can be found in Figure S4), where the Te peaks start to grow at around 160 °C, and the hybrid peaks vanish above 210 °C, mimicking an accelerated degradation process in ambient condition. Fig. 4B shows the results under N₂ protection (more spectra in Fig. S4). In this case, no or very little Te related Raman signal can be observed for temperature up to 300 °C; but at around 230 °C, ZnTe LO phonon starts to emerge (Fig. S4). When brought back to room temperature after heated up to 500 °C, the sample exhibits the characteristic multiple LO phonon resonant Raman modes of a somewhat defective ZnTe²⁸ (Fig. 4C), which is similar to the report where thermal annealing of ZnS(en)_{0.5} at 600 °C in vacuum yielded ZnS³². However, if heated in air, no ZnTe is found in the degradation product either at high temperature (up to 400 °C, Fig. 4A) or after returning to room temperature (Fig. 4D) where instead a mixture of Te and TeO₂ is seen³³. Thus, N₂ to a large extent prevents the oxidation process, and the process reflects the intrinsic degradation path: evaporation of en molecules. The finding provides guidance to the acceptable operation temperature of a potential device using this material with proper encapsulation to minimize the oxidation. The TGA results, shown in Fig. 4D, are qualitatively consistent with the spectroscopy results but offer more insight. Initially till around 230 °C, both

curves show slow mass reduction, but the curve in N₂ is slightly faster (inset of Fig. 4C), which can be explained by that while ligand evaporation or calcination occurs due to heating in both cases, in air the mass loss is made up partially by oxidation. The TGA curve in N₂ shows continual decrease but accelerated near 290 °C, reaching a plateau before 400 °C, corresponding to the complete conversion into ZnTe, which matches the mass loss of the molecules (about 13% in weight). In contrast, in air, significant mass loss does not occur until around 200 °C, and at about 290 °C, the curve actually begins to increase, reflecting the oxidation process is accelerated; and the mass gain saturates at around 600 °C. We may understand the intriguing curve as a convoluted effect of multiple competing oxidation processes: $\text{ZnTe}(\text{en})_{0.5} \rightarrow \text{ZnTeO}_2$, where ZnTeO₂ is predominantly a mixture of ZnO + xTe + yTeO + zTeO₂ (x + y + z = 1), where the highest point matches ZnO + 0.5Te + 0.5TeO₂. The detailed analyses are given in Fig. S4, although the exact degradation process requires further study. We may have a unified picture for the thermal degradation: following the initial loss of en near the surface, the molecules in the body start to leave at around 290 °C, and at close to 400 °C, the hybrid is fully degraded, resulting in different products in different environments.

Discussion

β -ZnTe(en)_{0.5} can be viewed as one of the most perfect man-made superlattices and the only hybrid superlattice that has been carefully investigated. It demonstrates a totally different consideration for forming a perfectly abrupt heterostructure, that is, combining two structures with drastically different materials, instead of two structurally similar ones, to eliminate the intermixing that occurs in most conventional heterostructures. It also represents a structure with unusual chemical bonding (i.e., 3-fold bonded Te atoms) yet without the detrimental effects of

dangling bonds. An inorganic analog is the abrupt interface between rock-salt PbTe and zinc-blende CdTe along their [111] direction³⁴.

Ultimately the long-term stability of an organic-inorganic hybrid is determined by the magnitude of the formation energy, although the kinetic barrier is also relevant. We performed DFT calculations for the formation energies of β -ZnTe(en)_{0.5} and ZnTe. They are -0.52 eV per formula for ZnTe(en)_{0.5}, compared to -0.80 eV for ZnTe (typical for II-VI compounds), and much greater than that of (CH₃NH₃)PbI₃ in the range of ± 0.1 eV^{11, 12}. However, when the formation energy is adequately high, extrinsic degradation paths could be practically more significant for the long-term stability of a hybrid. For the II-VI hybrid, ideally the surface is passivated by the organic molecules. Nevertheless, not all crystals are made equal, and their shelf life varied substantially with some showing very little sign of degradation up to 17 years. The deterioration of structural integrity is caused by the extrinsic effects, such as surface imperfection, exposed edge, and structural defects. By providing a comprehensive characterization of this prototype system, this work illustrates the interplay of these different factors in determining the long-term stability of an organic-inorganic hybrid material. Furthermore, it shows despite the structure complexity, a hybrid material can in fact have very high degree of crystallinity, manifested in both macroscopic structural properties (e.g., XRD) and microscopic properties (e.g., native defects). This attribute offers much needed quantum coherency for electronic processes in next generation (opto)electronic technologies.

Methods

Materials. Samples of β -ZnTe(en)_{0.5} were synthesized following slight modifications of previously reported literature procedures¹⁴. ZnCl₂ (333 mg, 2 mmol), Te (128 mg, 1 mmol), and

ethylenediamine (4 mL) were placed in a Teflon-lined stainless steel high pressure acid digestion vessel (Parr model 4746). The vessel was placed in a muffle furnace set at 200 °C for 10 days. After slow cooling to room temperature, the resulting product mixture was filtered and washed with distilled water, 95% ethanol and diethyl ether, then dried in air to produce colorless plate-like crystals.

Optical characterization. Raman and PL measurements were carried out on a Horiba LabRam HR800 confocal Raman microscope with a 1200g/mm grating. To excite Raman signal, a 532 nm laser beam was focused on the sample surface using a long working distance 50x microscope lens with NA = 0.5. The laser power focused onto the sample was $125 \pm 10 \mu\text{W}$. For PL, the sample was excited by a 325 nm laser beam, which was focused through a 40x UV microscope lens with NA = 0.5. Laser power delivered to the sample was 15.5 μW .

Structural characterization. X-ray crystallography data were acquired with an Agilent (now Rigaku) Gemini A Ultra diffractometer. Crystals of suitable size were coated with a thin layer of paratone-N oil, mounted on the diffractometer, and flash cooled to 105 K in the cold stream of the Cryojet XL liquid nitrogen cooling device (Oxford Instruments) attached to the diffractometer. The diffractometer was equipped with sealed-tube long fine focus X-ray sources with Mo target ($\lambda = 0.71073 \text{ \AA}$) and Cu target ($\lambda = 1.5418 \text{ \AA}$), four-circle kappa goniometer, and CCD detector. CrysAlisPro software was used to control the diffractometer and perform data reduction. The crystal structure was solved with SHELXS. All non-hydrogen atoms appeared in the E-map of the correct solution. Alternate cycles of model-building in Olex2 and refinement in SHELXL followed. All non-hydrogen atoms were refined anisotropically. All hydrogen atom positions were calculated based on idealized geometry and recalculated after each cycle of least

squares. During refinement, hydrogen atom – parent atom vectors were held fixed (riding motion constraint).

High resolution x-ray diffraction (HRXRD) measurements were performed at room temperature on an XRD diffractometer (PANalytical's X'Pert PRO) with triple-axis configuration using monochromatized Cu K α radiation (1.5418 Å). To compare the line shape of 2 θ - ω coupled scans and rocking curves, peak intensities were normalized, and the peak positions were centered at zero.

Surface analysis. The morphology of the hybrid samples was investigated by using scanning electron microscope (JEOL JSM-6480) equipped with x-ray energy dispersive spectrometry (EDX). EDX spectra were obtained with 10 keV beam energy.

X-ray photoelectron spectroscopy (XPS; Thermo Scientific ESCALAB XI+) was carried out using 200 μ m diameter monochromatized Al source ($h\nu = 1486.6$ eV). For depth profiling, sample surface was repeatedly sputtered with an argon beam (3000 eV, 500 μ m diameter) and analyzed by XPS. The etch rate was estimated to be 10 nm/s. Binding energies were calibrated relative to the C 1s peak at 284.8 eV.

Thermal study. Temperature-dependent Raman measurements were carried out with a heating system Linkam TS1500. At each temperature step, five minutes were allowed for thermal stabilization of the sample before Raman spectrum was measured. N₂ protected condition was achieved by a mild sustainable N₂ flow into the chamber during the entire temperature profile³⁵.

Thermogravimetric analysis was performed using Mettler Toledo TGA/SDTA851 instrument (Mettler-Toledo AG Analytical, Schwensenbach, Switzerland) in both air and N₂ surroundings.

Blanks were run under identical conditions for each gas and subtracted from the respective TGA curves to correct for buoyancy.

Density-functional theory modeling. Density functional theory (DFT) calculations were carried out using the Vienna ab initio simulation package (VASP)³⁶. The projector augmented wave potentials were used to describe the interaction between the ion-cores and valence electrons. The PBEsol generalized gradient approximation was used for the exchange–correlation functional. Plane-waves with cutoff energy of 50 Ry were used as basis set. The formation energy of ZnTe(en)_{0.5} was calculated by taking the total energy difference between bulk ZnTe(en)_{0.5} and the sum of zinc-blende ZnTe and C₂N₂H₈ molecule in the corresponding stoichiometry. Raman spectrum calculations (frequency and intensity) were carried out following *Ref. (37)*.

Data Availability

All data needed to evaluate the conclusions in the paper are present in the manuscript or the supplementary information. Additional data related to this paper may be requested from Y.Z. (yong.zhang@uncc.edu).

References

- 1 Mitzi, D. B. Synthesis, structure, and properties of organic-inorganic perovskites and related materials, in *Progress in Inorganic Chemistry* (ed Karlin) 1-121 (John Wiley & Sons, Inc., 1999).
- 2 Ishihara, T. Optical Properties of Pb-Based Inorganic-Organic Perovskites, in *Optical Properties of Low-Dimensional Materials* (eds T. Ogawa & Y. Kanemitsu) 289-339 (World Scientific, 1995).

- 3 Sanchez, C., Julián, B., Belleville, P. & Popall, M. Applications of Hybrid Organic–Inorganic Nanocomposites. *Journal of Materials Chemistry* **15**, 3559-3592 (2005).
- 4 Kickelbick, G. Introduction to Hybrid Materials, in *Hybrid Materials* (ed Guido Kickelbick) 1-48 (2007).
- 5 Liu, W., Fang, Y. & Li, J. Copper Iodide Based Hybrid Phosphors for Energy-Efficient General Lighting Technologies. **28**, 1705593 (2018).
- 6 Chen, Q. *et al.* Multiple-Stage Structure Transformation of Organic-Inorganic Hybrid Perovskite CH₃NH₃PbI₃. *Physical Review X* **6**, 031042 (2016).
- 7 Yang, S. *et al.* Stabilizing halide perovskite surfaces for solar cell operation with wide-bandgap lead oxysalts. *Science* **365**, 473-478 (2019).
- 8 Wang, Y. *et al.* Stabilizing heterostructures of soft perovskite semiconductors. *Science* **365**, 687-691 (2019).
- 9 Wang, R. *et al.* Constructive molecular configurations for surface-defect passivation of perovskite photovoltaics. *Science* **366**, 1509-1513 (2019).
- 10 Gratzel, M. The light and shade of perovskite solar cells. *Nat Mater* **13**, 838-842 (2014).
- 11 Tenuta, E., Zheng, C. & Rubel, O. Thermodynamic origin of instability in hybrid halide perovskites. *Scientific Reports* **6**, 37654 (2016).
- 12 Zhang, Y.-Y. *et al.* Intrinsic Instability of the Hybrid Halide Perovskite Semiconductor CH₃NH₃PbI₃. *Chinese Physics Letters* **35**, 036104 (2018).

- 13 Huang, X. Y., Li, J. & Fu, H. X. The first covalent organic-inorganic networks of hybrid chalcogenides: Structures that may lead to a new type of quantum wells. *Journal of the American Chemical Society* **122**, 8789-8790 (2000).
- 14 Huang, X. Y., Li, J., Zhang, Y. & Mascarenhas, A. From 1D chain to 3D network: Tuning hybrid II-VI nanostructures and their optical properties. *Journal of the American Chemical Society* **125**, 7049-7055 (2003).
- 15 Esaki, L. & Tsu, R. *IBM Res. Dev.* **14**, 61 (1970).
- 16 Li, J. H. *et al.* Layer ordering and faulting in (GaAs)_n/(AlAs)_n ultrashort-period superlattices. *Physical Review Letters* **91**, 106103 (2003).
- 17 Zhang, Y. *et al.* Zero Thermal Expansion in a Nanostructured Inorganic-Organic Hybrid Crystal. *Physical Review Letters* **99**, 215901-215904 (2007).
- 18 Zhang, Y. *et al.* Novel Approach to Tuning the Physical Properties of Organic-Inorganic Hybrid Semiconductors. *Physical Review Letters* **96**, 026405-026404 (2006).
- 19 Qian, X., Gu, X. & Yang, R. Thermal conductivity modeling of hybrid organic-inorganic crystals and superlattices. *Nano Energy* **41**, 394-407 (2017).
- 20 Li, J., Bi, W. H., Ki, W., Huang, X. Y. & Reddy, S. Nanostructured crystals: Unique hybrid semiconductors exhibiting nearly zero and tunable uniaxial thermal expansion behavior. *Journal of the American Chemical Society* **129**, 14140 (2007).
- 21 Mak, K. F., Lee, C., Hone, J., Shan, J. & Heinz, T. F. Atomically Thin MoS₂: A New Direct-Gap Semiconductor. *Physical Review Letters* **105**, 136805 (2010).
- 22 Sun, Y. *et al.* Fabrication of flexible and freestanding zinc chalcogenide single layers. *Nature Communications* **3**, 1057 (2012).

- 23 Reshchikov, M. A. & Morkoç, H. Luminescence properties of defects in GaN. **97**, 061301 (2005).
- 24 Özgür, Ü. *et al.* A comprehensive review of ZnO materials and devices. **98**, 041301 (2005).
- 25 Giorgini, M. G., Pelletti, M. R., Paliani, G. & Cataliotti, R. S. Vibrational spectra and assignments of ethylene-diamine and its deuterated derivatives. **14**, 16-21 (1983).
- 26 Deng, Z. X., Li, L. B. & Li, Y. D. Novel inorganic-organic-layered structures: Crystallographic understanding of both phase and morphology formations of one-dimensional CdE (E = S, Se, Te) nanorods in ethylenediamine. *Inorganic Chemistry* **42**, 2331-2341 (2003).
- 27 Pine, A. S. & Dresselhaus, G. Raman Spectra and Lattice Dynamics of Tellurium. *Physical Review B* **4**, 356-371 (1971).
- 28 Yi, Y. *et al.* Intrinsic Exciton-Phonon Coupling and Tuning in ZnTe Nanowires Probed by Resonant Raman Scattering. *Physical Review Applied* **13**, 011001 (2020).
- 29 Kung, P. *et al.* High quality AlN and GaN epilayers grown on (00·1) sapphire, (100), and (111) silicon substrates. **66**, 2958-2960 (1995).
- 30 Lu, P. & Smith, D. J. The observation of in situ and ex situ oxidation processes for ZnTe surfaces by high-resolution electron microscopy. **107**, 681-691 (1988).
- 31 Kita, A., Ozawa, M. & Gutleben, C. D. XPS analysis of chemically etched II–VI semiconductor surfaces. *Applied Surface Science* **100-101**, 652-655 (1996).
- 32 Liu, J. *et al.* Novel porous single-crystalline ZnO nanosheets fabricated by annealing ZnS(en)_{0.5}(en = ethylenediamine) precursor. Application in a gas sensor for indoor air contaminant detection. *Nanotechnology* **20**, 125501 (2009).

- 33 Ceriotti, M., Pietrucci, F. & Bernasconi, M. Ab initio study of the vibrational properties of crystalline TeO₂: The α , β , and γ phases. *Physical Review B* **73**, 104304 (2006).
- 34 Zhang, B. *et al.* Quantum Oscillations in a Two-Dimensional Electron Gas at the Rocksalt/Zincblende Interface of PbTe/CdTe (111) Heterostructures. *Nano Letters* **15**, 4381–4386 (2015).
- 35 Su, L. & Zhang, Y. Temperature coefficients of phonon frequencies and thermal conductivity in thin black phosphorus layers. *Applied Physics Letters* **107**, 071905 (2015).
- 36 Kresse, G. & Furthmüller, J. Efficient iterative schemes for ab initio total-energy calculations using a plane-wave basis set. *Physical Review B* **54**, 11169-11186 (1996).
- 37 Umari, P., Pasquarello, A. & Dal Corso, A. Raman scattering intensities in α -quartz: A first-principles investigation. *Physical Review B* **63**, 094305 (2001).
- 38 Itkin, V. P. & Alcock, C. B. The O-Te (oxygen-tellurium) system. *Journal of Phase Equilibria* **17**, 533-538 (1996).

Acknowledgements

We thank Dr. Kristen Dellinger of UNCG for assistance in XPS measurements, Dr. Jianhua Li of Rice Univ. and Zahirul Islam of ANL for single crystal XRD measurements, Dr. Haitao Zhang of UNCC in SEM/EDX measurements, and Dr. Brian Fluegel of NREL for locating some aged samples. The work at UNCC was supported by ARO/Physical Properties of Materials (Grant No. W911NF-18-1-0079), University of North Carolina's Research Opportunities Initiative (UNC ROI) through Center of Hybrid Materials Enabled Electronic Technology, and Bissell Distinguished Professorship.

Author contributions

Y.Z. and T.S. conceived the idea and led the project. M.K., A.N., T.M., X.H., and J.L. performed the material syntheses; T.Y. and Y.Z. conducted optical measurements; F.Z., T.Y., M.K. and D.S.J. performed XRD measurements; F.Z., T.Y., M.K., and D.B. performed SEM/EDX measurement; T.Y. and M.K. performed XPS measurements; Y.S. performed DFT calculations. Y.Z., T.Y, T.M., and M.K. wrote the manuscript. All authors discussed the results and commented on the manuscript.

Competing interests

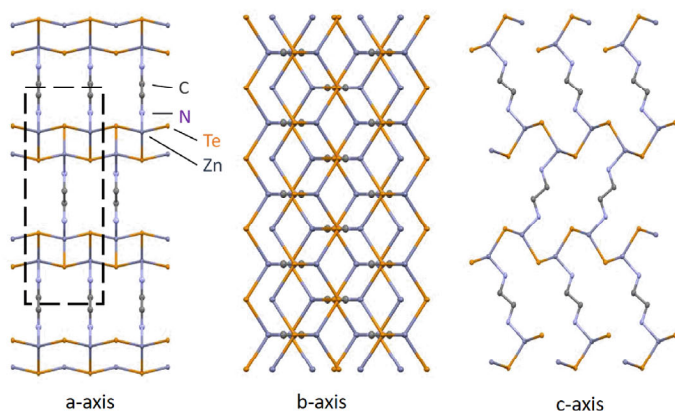
None declared.

Materials & Correspondence

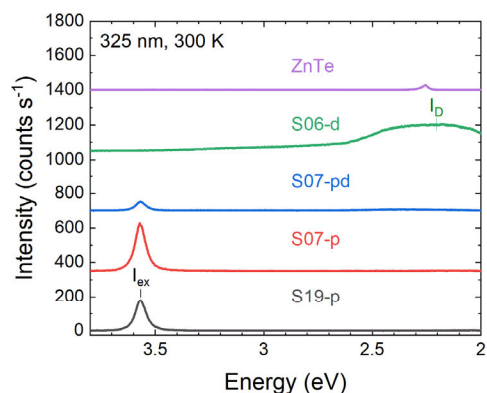
Correspondence and requests for materials should be addressed to Y.Z. (yong.zhang@uncc.edu).

Figures

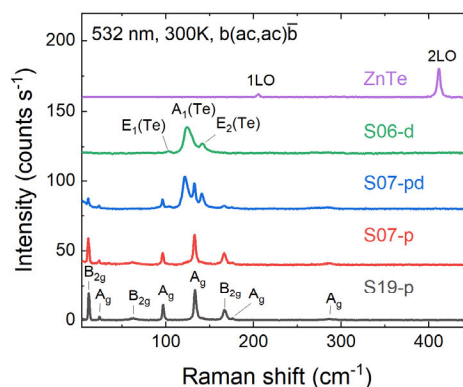
a



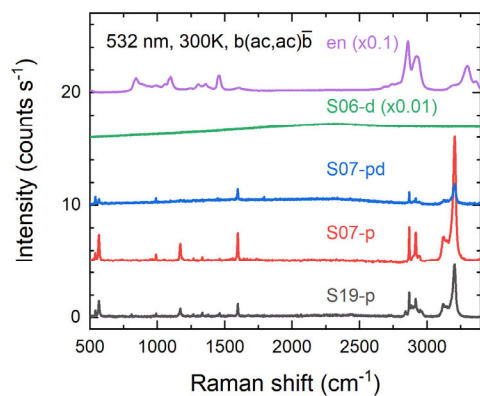
b



c



d



e

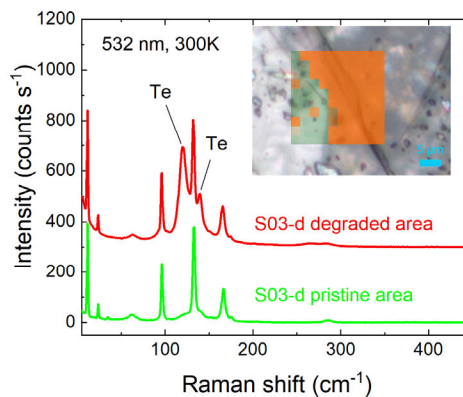


Fig. 1. Optical spectroscopy signatures of $\beta\text{-ZnTe(en)}_{0.5}$ at different degradation stages. a, Crystal structure viewed along 3 axes. **b,** Photoluminescence spectra. **c,** Raman spectra of low wavenumber region. **d,** Raman spectra of large wavenumber region. **e,** Raman spectra of pristine and partially degraded areas adjacent to each other (inset: Raman mapping of the Te mode showing no sign of degradation in the green area but partial degradation in the red area).

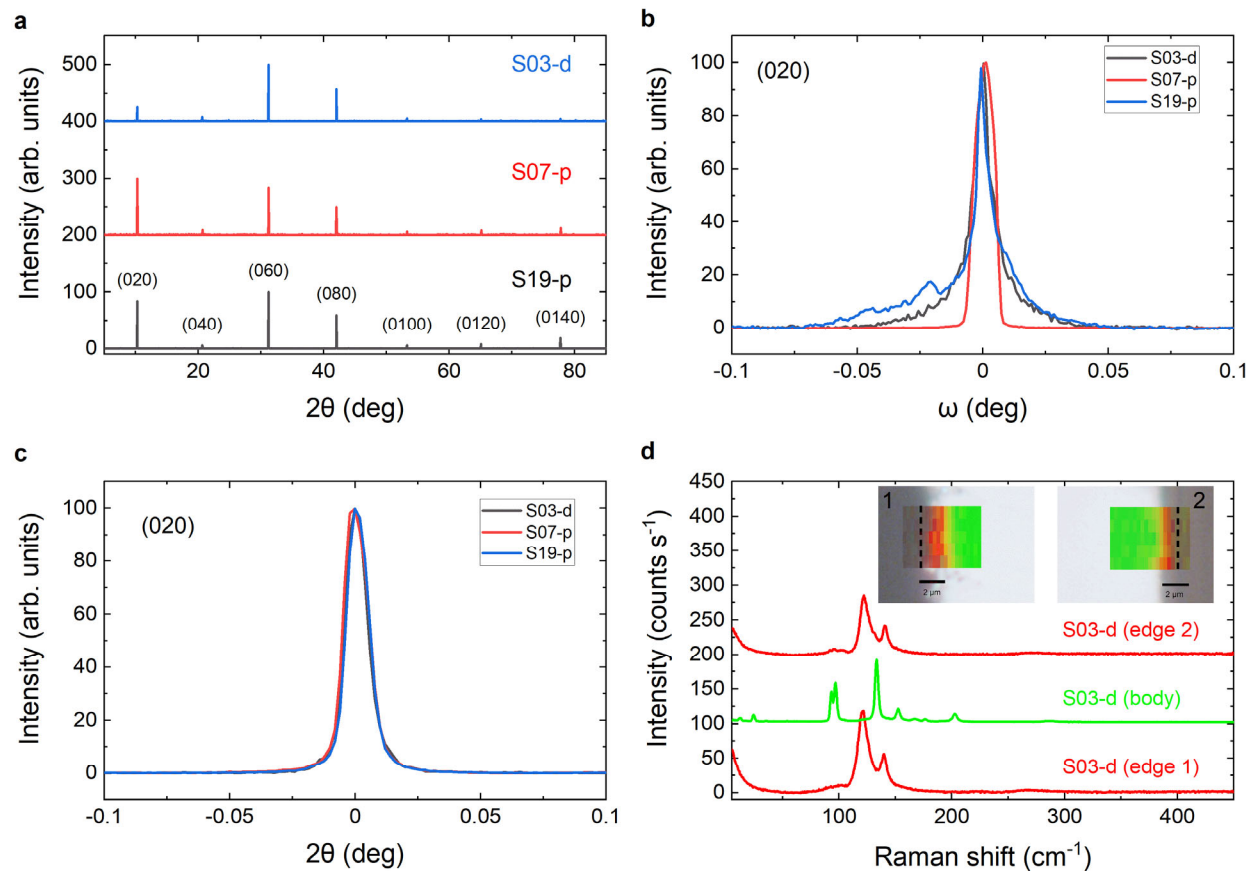


Fig. 2. XRD and Raman characterization of pristine and seemingly degraded samples. a, b axis XRD 2θ scans for S19-p, S07-p, and S03-d. **b,c**, High-resolution XRD rocking curves or ω scans and 2θ scans, respectively, at (0,2,0) reflection for the three samples. **d**, Raman spectra of S03-d measured from the cleaved edge at locations close and away from the surfaces (insets: Raman mapping of the Te mode, overlaid with the optical image, on the cleaved edge near the upper and lower surface of the crystal, where the dashed lines indicate the sample surfaces).

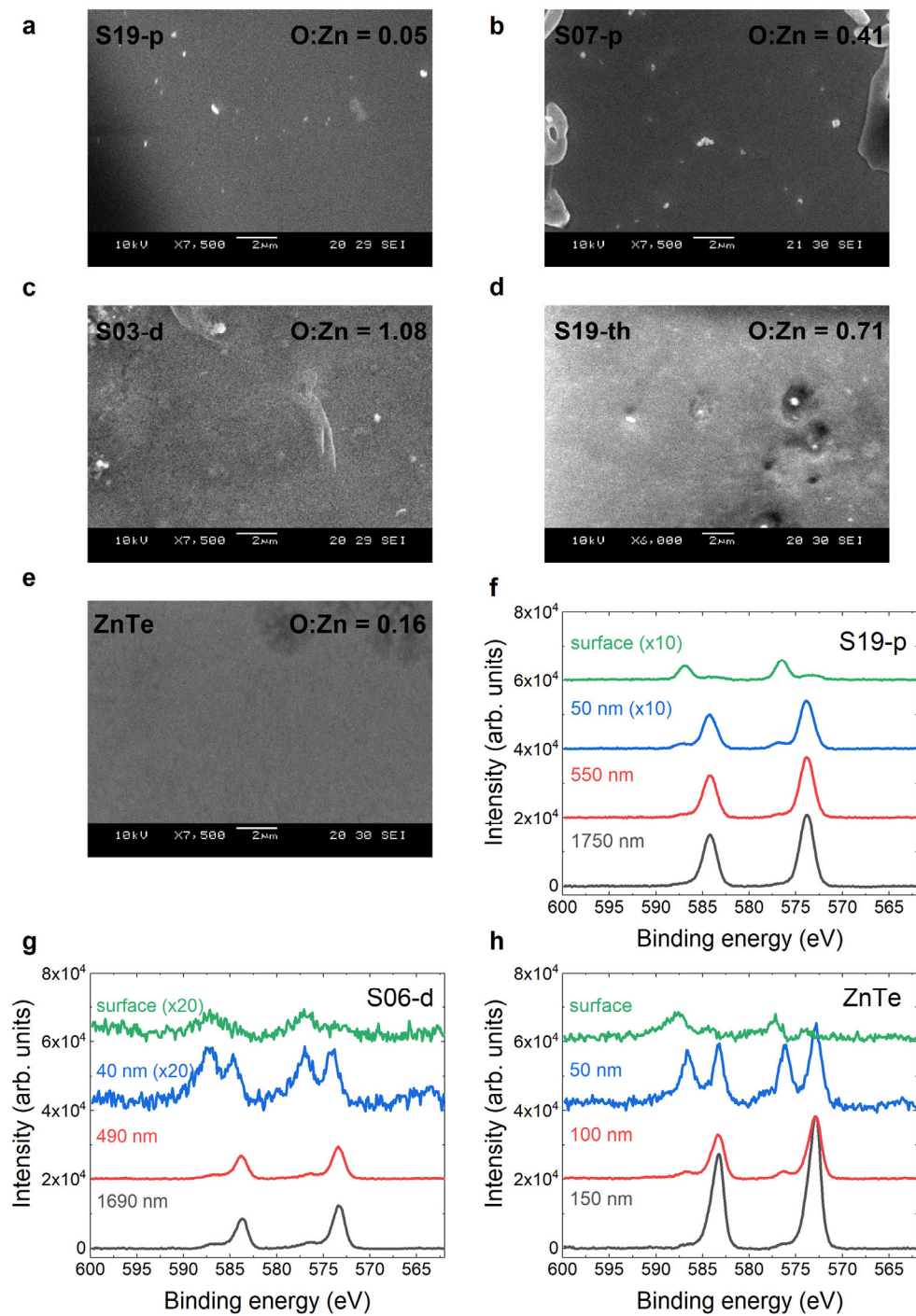


Fig. 3. SEM and XPS surface characterization and analyses. a–e, SEM images of a fresh sample (S19-p) (a), an aged sample showing very little degradation optically (S07-p) (b), an aged sample optically showing severe degradation (S03-d) (c), a thermally degraded fresh sample (S19-th) (d), and single crystalline ZnTe (e). f–h, XPS spectra at different etching times or depths of sample S19-p (f), sample S06-d (g) and ZnTe (h).

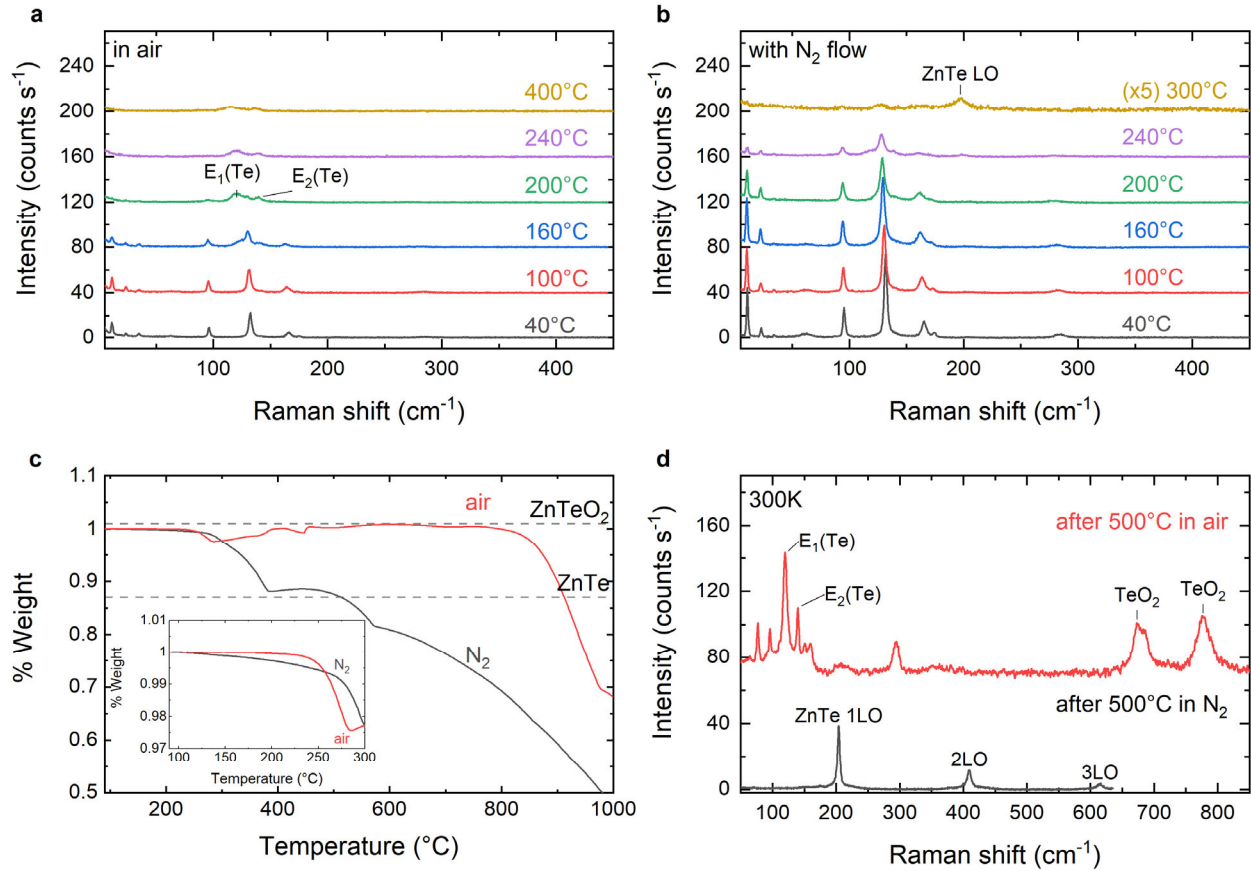
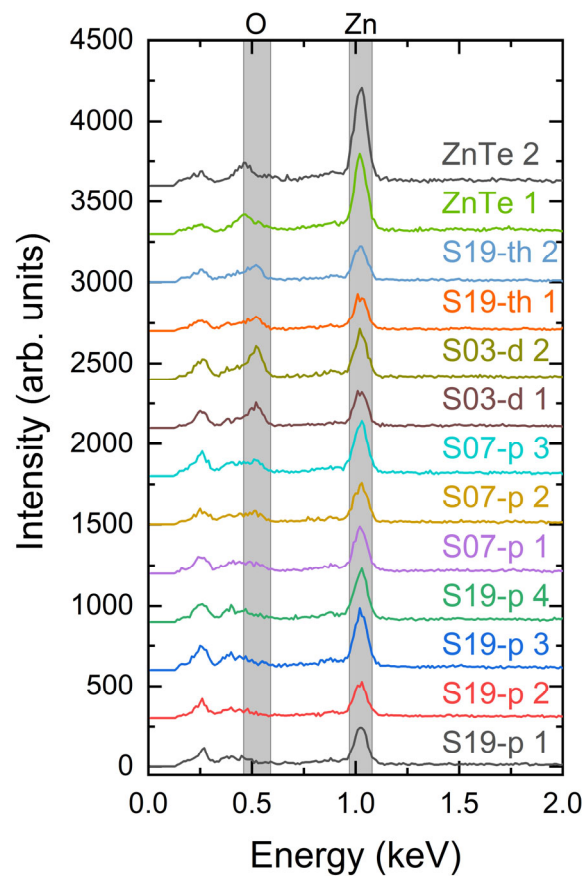


Fig. 4. Thermal degradation of freshly made sample (S19-p) in air and N₂ environment probed by Raman and thermogravimetric analysis (TGA). a, In-situ Raman spectroscopy in air. **b,** In-situ Raman spectroscopy in N₂. **c,** TGA in air and N₂ (inset: low temperature region). **d,** Raman spectra at room temperature after being heated to 500 °C in air and N₂ then returning to room temperature.

Supplementary information

Fig. S1.

a



b

	Mean	Std Dev
ZnTe	0.16	0.04
S19-p	0.05	0.02
S07-p	0.41	0.04
S03-d	1.08	0.07
S19-th	0.71	0.11

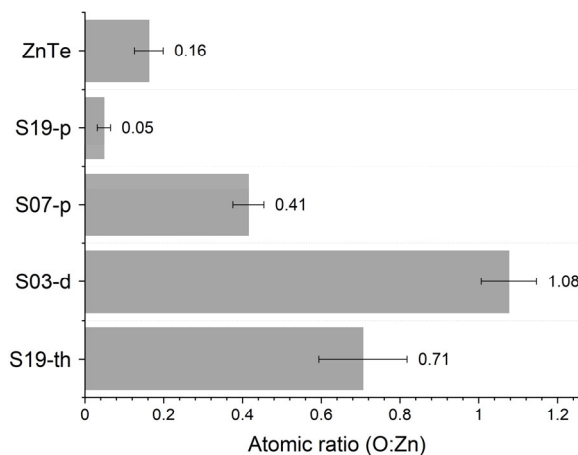


Fig. S1. EDX and atomic ratio analysis. a, EDX spectra of different samples. b, Atomic ratios of O:Zn obtained from integrated peak intensities of EDX spectra after background subtraction.

Fig. S2.

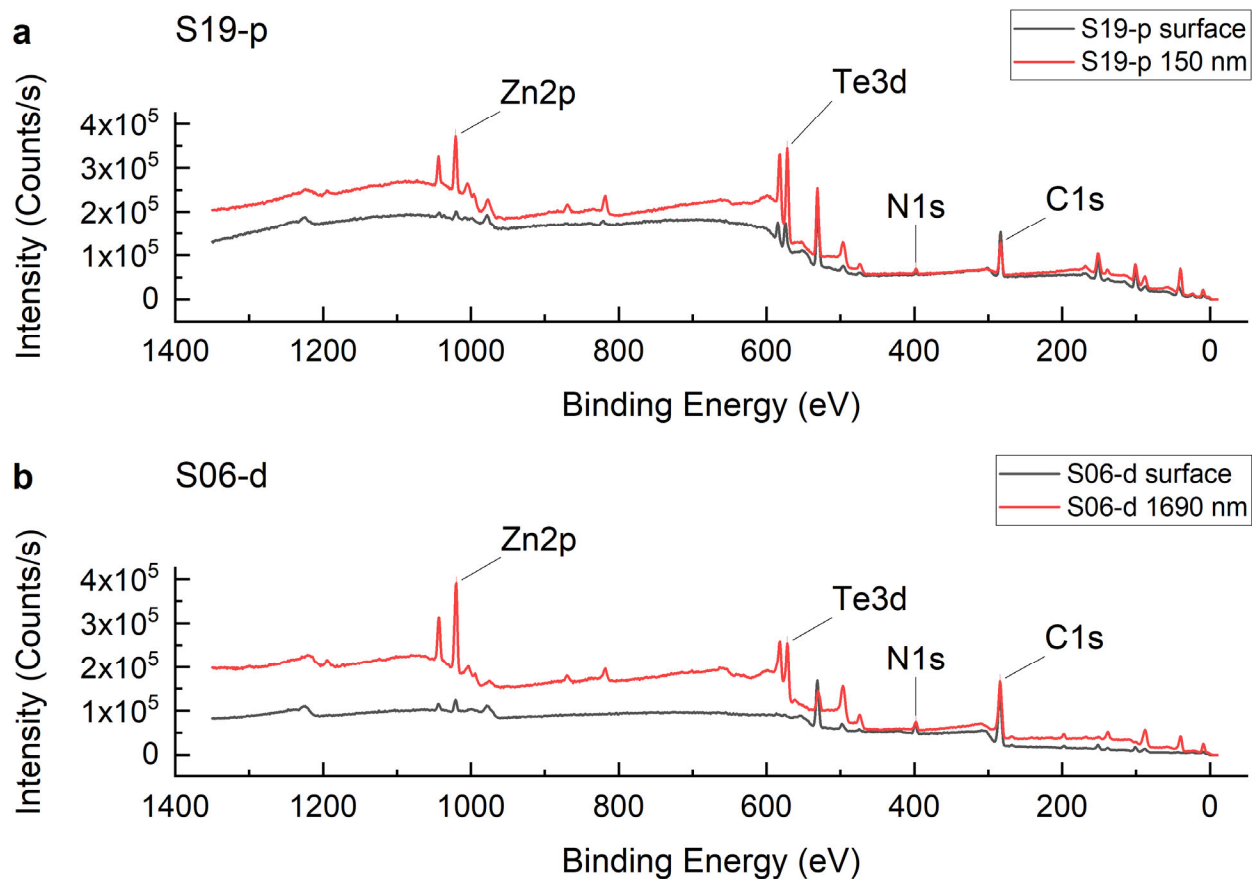


Fig. S2. XPS spectra at different etching times or depths in an extended spectral range. a pristine sample S19-p **(a)** and an optically degraded sample S06-d **(b)**.

Fig. S3.

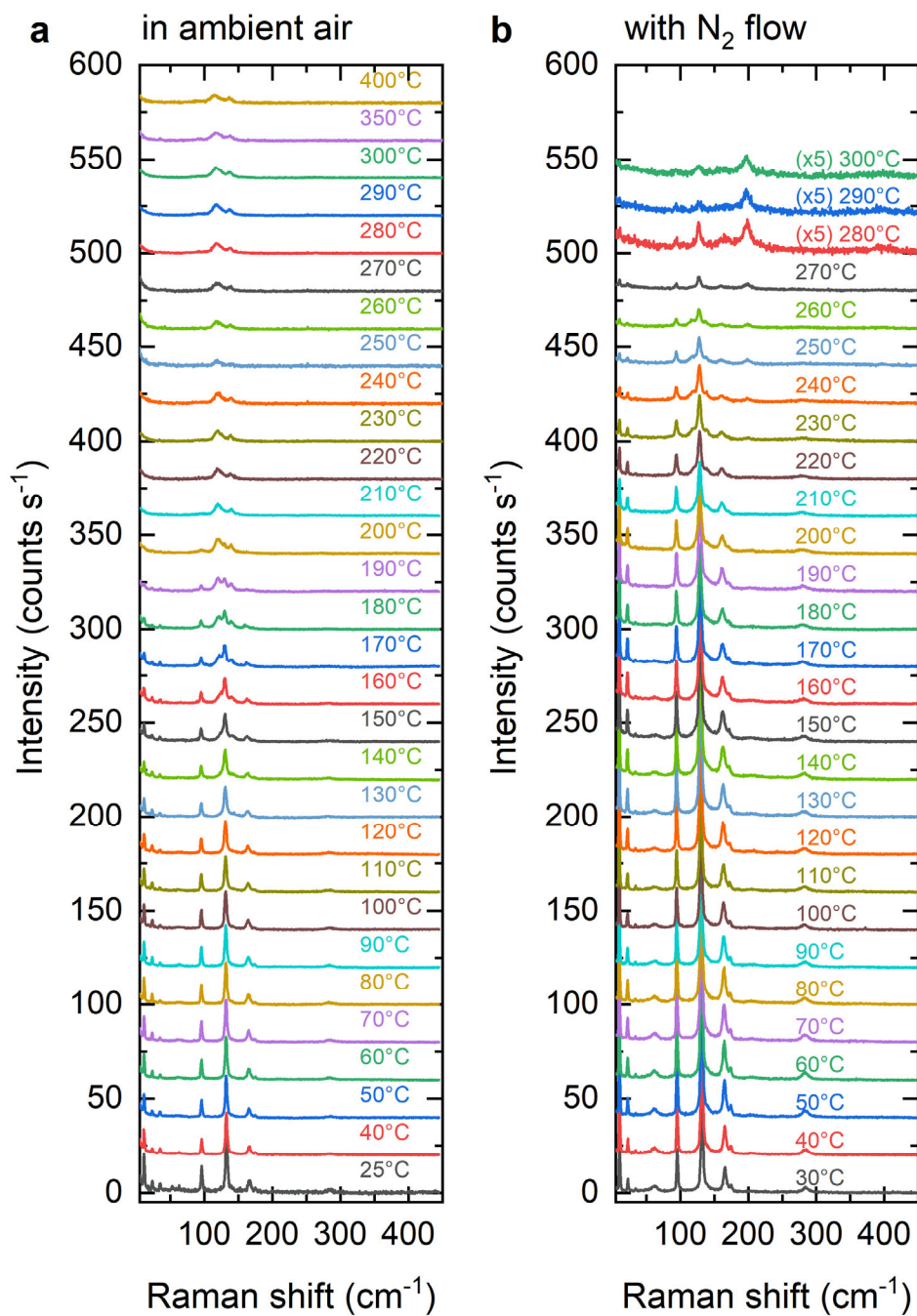
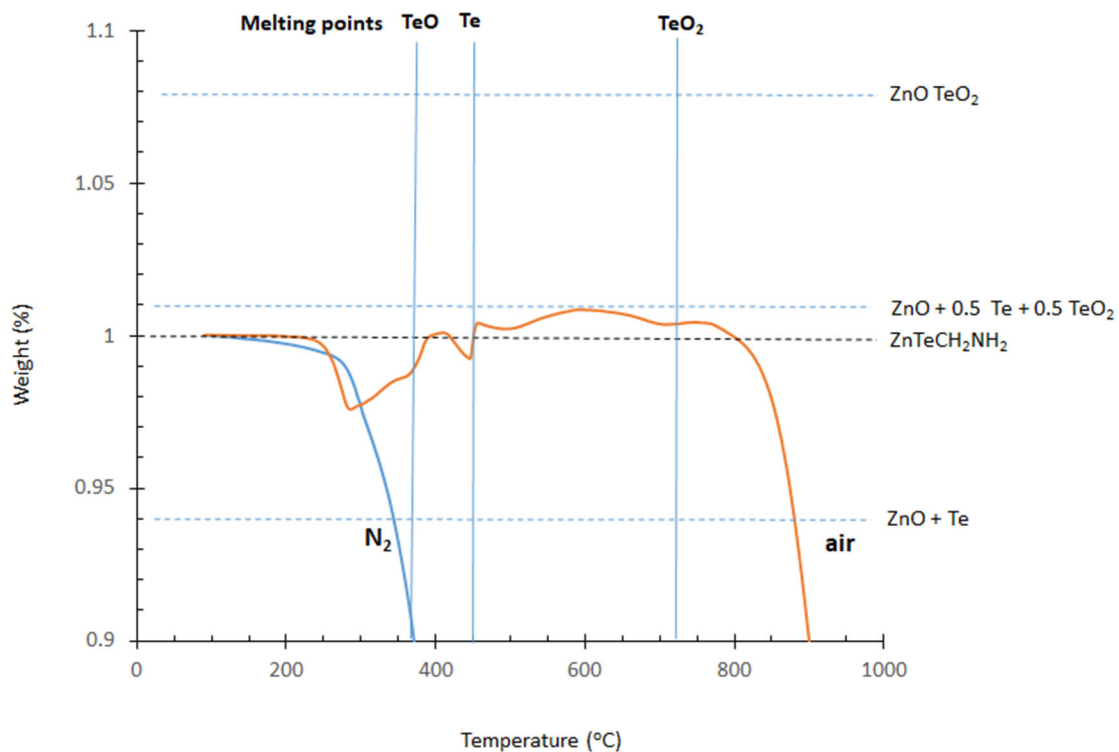


Fig. S3. In-situ heating studies using Raman spectroscopy for a freshly made sample S19-p in air (a) and N₂ (b).

Fig. S4.



Formula	MW	Relative mass
ZnTe(CH ₂ NH ₂)	223.0296	1.00
ZnTeO ₃	240.9782	1.08
ZnTeO ₂	224.9788	1.01
ZnTeO	208.9794	0.94
ZnTe	192.98	0.87

Fig. S4. Analyses of TGA curves for a freshly made sample S19-p in air and N₂. Horizontal lines indicate the masses of different potential degradation products, with the values show in the table below. The vertical lines indicate the melting temperatures for different Te products: 370, 450, and 720 °C for TeO, Te, and TeO₂, respectively ³⁸.

Table S1.

Observed Raman modes and their symmetry assignments.

Fig.	Wave number (cm⁻¹)	Symmetry	Corresponding mode of en
1c	12.11	B2g	
1c	24.26	Ag	
1c	62.61		
1c	96.88	Ag	
1c	133.38	Ag	
1c	167.09	B2g	
1c	175.22	Ag	
1c	286.74	Ag	
1d	540.71	Ag	
1d	567.03	B2g	
1d	988.53	Ag	
1d	1170.35	Ag	
1d	1596.71	Ag	
1d	2868.82	Ag	C-H vibration (2860 cm ⁻¹)
1d	2916.37	B2g	C-H vibration (2928 cm ⁻¹)
1d	3128.44	Ag	
1d	3203.68	B2g	

Table S2.

Powder diffraction analyses of a pristine sample S19-p and an optically degraded sample S06-d, yielding nearly identical (a , b , c) lattice constants.

	S19-p	S06-d	Ref. (13)	Ref. (17)
a (Å)	5.6709(9)	5.6736(6)	5.660(1)	5.6787(2)
b (Å)	17.160(3)	17.169(2)	17.156(3)	17.1998(6)
c (Å)	4.3403(6)	4.3445(5)	4.336(1)	4.3523(1)
α, β, γ	90°	90°	90°	90°
Volume (Å³)	422.37(12)	423.21(9)	421.04(14)	425.10(4)
$R1$, obs.	0.0371	0.0365	0.0495	
$wR2$, obs.	0.0766	0.0896	0.0816	

Table S3.

XRD (0,n,0) reflection peak relative intensities, normalized to (0,6,0). Simulated intensities were calculated from S19-p single-crystal structure data (using Mercury 3.10.2, CCDC).

h	k	l	S19-p	S07-p	S03-d	Simulated
0	2	0	84.2	119	27.2	75.1
0	4	0	5.72	10.4	8.02	7.02
0	6	0	100	100	100	100
0	8	0	59.6	59.4	57.4	63.7
0	10	0	5.72	7.29	5.56	6.82
0	12	0	7.69	9.38	3.7	6.41
0	14	0	18.3	14.6	4.94	16.3

Simulated XRD spectrum of (0,n,0) reflections:

